Molecular dynamics simulations of radiation damage in YBa2Cu3O7

Gray, R L; Rushton, M J D; Murphy, S T

Superconductor Science and Technology

DOI:
10.1088/1361-6668/ac47dc

Published: 07/02/2022

Publisher's PDF, also known as Version of record

Molecular dynamics simulations of radiation damage in $YBa_2Cu_3O_7$

OPEN ACCESS
IOP Publishing
Superconductor Science and Technology
Supercond. Sci. Technol. **35** (2022) 035010 (16pp)
https://doi.org/10.1088/1361-6668/ac47dc

Molecular dynamics simulations of radiation damage in $YBa_2Cu_3O_7$

R L Gray[1], M J D Rushton[2] and S T Murphy[1,*]

[1] Engineering Department, Lancaster University, Bailrigg, Lancaster LA1 4YW, United Kingdom
[2] Nuclear Futures Institute, Bangor University, Bangor, Gwynedd LL57 2DG, United Kingdom

E-mail: samuel.murphy@lancaster.ac.uk

Received 22 September 2021, revised 20 December 2021
Accepted for publication 4 January 2022
Published 7 February 2022

Abstract

The advent of high-temperature superconductors (HTS) with high field strengths offers the possibility of building smaller, cheaper magnetically confined fusion reactors. However, bombardment by high energy neutrons ejected from the fusion reaction may damage the HTS tapes and impair their operation. Recreating the conditions present in an operational fusion reactor is experimentally challenging, therefore, this work uses molecular dynamics simulations to understand how radiation modifies the underlying crystal structure of $YBa_2Cu_3O_7$. To facilitate the simulations a new potential was developed that allowed exchange of Cu ions between the two symmetrically distinct sites without modifying the structure. Radiation damage cascades predict the formation of amorphous regions surrounded by regions decorated with Cu and O defects found in the CuO-chains. The simulations suggest that the level of recombination that occurs is relatively low, resulting in a large number of remnant defects and that there is a no substantial temperature effect.

Keywords: $YBa_2Cu_3O_7$, radiation damage, molecular dynamics

(Some figures may appear in colour only in the online journal)

1. Introduction

Nuclear fusion offers the prospect of large quantities of low carbon energy, without producing very long-lived radioactive waste, while simultaneously avoiding safety and proliferation issues inherent in today's fission reactors. Based on the Lawson criteria, the reaction between deuterium and tritium is the most suitable for energy generation from fusion. In order to overcome the Coulombic repulsion between the nuclei requires confining the fusion plasma and heating it to in excess of 100 m K [1, 2]. Within magnetic confinement fusion (MCF), a plasma containing tritium and deuterium, is confined in a magnetic field in either a tokamak or a stellarator. One of the key factors influencing the efficacy of plasma confinement in MCF is the strength of the magnetic field itself. While early tokamaks employed copper magnets, more modern devices, such as ITER are exploiting the first generation of superconducting materials such as Nb_3Sn. Since ITER's design, the development of superconducting tapes made from high-temperature superconductors (HTS), such as the rare-earth barium cuprates ($REBa_2Cu_3O_{7-x}$), has enabled the development of magnets with significantly greater field strengths that can operate at higher temperatures. The increased field strength and reduced cooling requirement allow the construction of more compact tokamak reactors, and therefore they are considered to be a breakthrough technology in fusion development [3–5].

As it is not charged, the 14.1 MeV neutron released by the D–T reaction is not constrained within the magnetic field. These high energy neutrons are required for tritium breeding and their kinetic energy is converted into heat for

* Author to whom any correspondence should be addressed.

electricity generation, however, they will also damage the reactor components, including the magnets. As a consequence, it is necessary to understand how this neutron irradiation will change the atomic structure of a $REBa_2Cu_3O_7$ tape and alter the superconducting properties of the magnets during operation to enable development of appropriate shielding.

Neutrons transfer energy through elastic collisions with the atoms that constitute a material. If the energy transferred to an atom is greater than a, material dependent, threshold displacement energy, t_d, the atom is displaced. Previous estimates for the threshold displacement energy for oxygen in $YBa_2Cu_3O_7$ are in the range 4.2–18.8 eV [6]. This atom can then displace other atoms leading to a collision cascade. Following this initial, ballistic phase there is a recombination phase were displaced atoms may return to an equivalent site, thereby annealing some of the damage created. Defect recombination is highly dependent on the mobility of the constituent species. In $YBa_2Cu_3O_7$ the oxygen ions are expected to be highly mobile [7], while the Ba and Y cations exhibit high activation energies. In anycase, it might be expected that the recombination phase is unlikely to be effective at the operating temperatures of fusion magnets where temperatures are on the order of 25 K.

Previous fast neutron irradiation studies of $REBa_2Cu_3O_7$ indicate that there is initially a linear decrease in the critical temperature, T_c, and an in increase in the critical current density with fluence. This increase differs in the individual Cartesian directions, however, this serves to reduce the anisotropy resulting from the underlying crystal structure [8]. The increase is attributed to the introduction of nanoscale defect regions that can immobilize magnetic flux vortices thereby reducing pseudo-resistance due to flux creep. Chudy *et al* [9] argue that the point like defects have a significant impact on J_c, while the larger defective regions have a greater impact on the critical temperature. As the fluence increases the superconducting properties start to decrease due to saturation of pinning centres and the loss of the underlying crystal structure, particularly the CuO_2 planes [8, 10].

Many of these previous neutron irradiation experiments have been performed in the TRIGA reactor in Vienna, where the temperature is roughly 360 K. There are concerns that this temperature is not representative of reactor operating conditions, limiting applicability for understand the evolution of the superconducting properties during operation. As performing high fluence neutron irradiation at operational temperatures is very challenging, there is an emphasis on trying to understand the possible differences due to temperature using other approaches. Ion irradiation is often employed as a simulant for neutron irradiation and has been used to examine the evolution of the superconducting properties of $GdBa_2Cu_3O_7$ at operational temperatures. This study shows that there is a similar reduction in J_c and T_c at operational and room temperatures for most samples. The authors also note a significant recovery of J_c and T_c in samples irradiated at operational temperatures and left to anneal at room temperature [11].

In addition to use as a surrogate for neutron irradiation, ion irradiation is widely used to manipulate the superconducting properties of HTS, see for example [12–16]. The defects introduced depend on the energy of the incoming projectile, with lower energy light ions resulting in the formation of uncorrelated point defects and defect clusters, while heavy ions lead to the formation of correlated ion tracks [17]. The columnar defects act as efficient flux pinning centres, however, the pinning is highly anisotropic [18]. In contrast, the pinning effects of the point defects and clusters is less efficient although the effect is less anisotropic. Transmission electron microscopy (TEM) of Y(Dy)BCO films annealed after irradiation with 18 MeV Au ions has shown some recombination of oxygen vacancies in the CuO_2 planes, resulting in partial recovery of T_c and the self-field [19].

Molecular dynamics (MD) is an atomistic simulation technique that uses Newton's equations of motion to evolve a system of atoms in time. MD has been widely used to study radiation damage in materials using the primary knock-on atom (pka) method, offering an atomic level description of the complex defect morphology resulting from the impact of a high energy particle [20–22]. Radiation damage arising due to swift heavy ions (SHI) irradiation can also be simulated using MD, although not using the pka method outlined here, for more details see [23, 24].

Previous applications of MD for the study of low energy damage events in $YBa_2Cu_3O_7$ appear to suggest that there is a preference for damage on the oxygen sublattice [25], which correlates with the very low threshold displacement energies mentioned above. These simulations also support previous assertions that there is a high degree of anisotropy in the material's response to irradiation with preferential oxygen redistribution expected [26]. One of the major advantages of MD is the ability to easily control the temperature of the underlying lattice that is the target for the incoming projectile. Therefore, the objective of this work is to use molecular dynamics to understand the differences in the evolution of radiation damage cascades in $YBa_2Cu_3O_7$ at the temperatures present during the existing irradiation experiments and those at the operating temperatures relevant to a future reactor and to identify the dominant types of defects formed.

2. Crystallography

The rare earth barium cuprates exhibit complex anisotropic crystal structures as illustrated in figure 1. The unit cell is orthorhombic and is described using the *pmmm* [47] space group. A key feature of the rare-earth cuprate unit cell is the two symmetrically distinct Cu sites. The Cu1 site has the Wyckoff symbol 1 *a* and sits in the so-called Cu–O chains evident at the base of the unit cell in figure 1. The Cu2 ions occupy the 2 *y* Wyckoff site and bond to five oxygen ions forming a square-based pyramid. The base of the pyramid forms the CuO_2 chains that are thought to play an important role in the superconductivity of the material. Importantly, the copper ions residing on these sites are thought to exhibit different charge states, with the Cu1 site hosting a Cu^{3+} ion and Cu2 site hosting a Cu^{2+} ion.

Another important feature of cuprate superconductors is their ability to accommodate significant deviations in stoichiometry, i.e. $REBa_2Cu_3O_{7-\delta}$, where, δ can range from 1

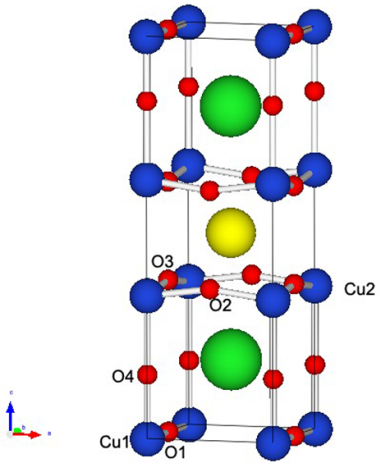

Figure 1. The crystal structure of $YBa_2Cu_3O_7$. Colour coded with O as red, Ba as green, Y as yellow and Cu as blue.

to 0. As δ decreases so does T_C, the critical temperature below which the material exhibits superconducting properties [27]. The oxygen deficiency is accommodated by oxygen vacancy defects that are thought to preferentially exist in the CuO-chains [28–30].

3. Methodology

3.1. Potential development

The predictive ability of classical MD simulations depends on the reliability of the empirical potential model used to describe the interactions between the atoms in the crystal. In particular, in rare-earth cuprate material it is important to be able to accurately describe the different copper environments discussed above. The complication is that Cu displays different charges based on where it sits in the crystal, however, in an MD simulation the charges are assigned at the start and remain fixed. Therefore, if a Cu ion moves from a Cu1 site to the Cu2 site it will retain its 3+ charge state. The introduction of Cu^{3+} ions into the CuO_2 planes will distort the crystal in a non-physical way and artificially modify the response of the crystal due to radiation damage. Charge transfer schemes do exist, for example QEQ [31] and ReaxFF [32], but these may be unreliable in the early stages of the cascade where the system is far from equilibrium as well as being computationally expensive.

There have been a number of potential models derived for $YBa_2Cu_3O_7$ including those of Chaplot [33] and Baetzold [34]. These potentials model the different Cu environments by either assigning different charges to the Cu ions on the two sites or by applying an extra potential term to atoms in the Cu–O chains. This clear distinction between the types of Cu ions is appropriate for the study of bulk properties, however, it is entirely unsuitable for dynamic simulations where these ions can swap sites, which will likely occur during a cascade. Despite this, the Chaplot potential has previously been applied to study cascades in $YBa_2Cu_3O_7$, but in this case all Cu–O interactions were assumed to be the same [35]. Used in this way the Chaplot potential offers a poor description of the $YBa_2Cu_3O_7$ system: it predicts a high oxygen diffusivity and the b and c lattice parameters are also underestimated, as will be discussed. Given the limitations of the existing models, a new potential must be developed for $YBa_2Cu_3O_7$ where the exchange of Cu ions between sites does not artificially distort the evolution of the lattice.

The new potential will take the general form:

$$E_i = \frac{1}{2}\sum_j \phi_{\alpha\beta}(r_{ij}) \tag{1}$$

$$\phi_{\alpha\beta}(r_{ij}) = \phi_C(r_{ij}) + \phi_B(r_{ij}) \tag{2}$$

$$\phi_C(r_{ij}) = \frac{q_\alpha q_\beta}{4\,\pi\epsilon_0 r_{ij}} \tag{3}$$

$$\phi_B(r_{ij}) = A_{\alpha\beta}\exp\left(\frac{-r_{ij}}{\rho_{\alpha\beta}}\right) - \frac{C_{\alpha\beta}}{r_{ij}^6}. \tag{4}$$

In equation (1) i and j are atom labels, $\phi_{\alpha\beta}(r_{ij})$. Equation (2) shows that the overall interaction is described as a combination of the Coulomb potential (equation (3)) and the Buckingham potential (equation (4)) [36], which is itself a combination of the Born–Mayer repulsive short range interaction [37] and the London dispersion forces [38]. The r_0 is found by averaging the bond lengths between the relevant species in the perfect structure.

In equation (3), q_α and q_β represent the charges on the ions, ϵ_0 is the permittivity of free space and the constants $A_{\alpha\beta}$, $\rho_{\alpha\beta}$ and $c_{\alpha\beta}$ are potential parameters specific to the ion pair α and β. For computational tractability, the Coloumb long range solver and Buckingham contributions were truncated with a cutoff of 12 Å. The Coulombic interactions were calculated using the particle–particle particle–mesh (PPPM) version of the Ewald summation [39].

During radiation damage cascades the ions can reach smaller ionic separations than under equilibrium conditions. Therefore, the Ziegler–Biersack–Littmark (ZBL) potential [40], which offers a better description of the shielded nuclear-nuclear interactions, is splined onto the Buckingham potential at short separations. Splining was performed using the atsim.potentials package [41].

3.2. Potential fitting

To fit potential parameters the lattice parameters and elastic constants calculated using LAMMPs [42] and GULP [43] and compared with a training database developed using density functional theory (DFT) to create a merit function. The potential parameters were then optimised simultaneously using the 'Potential Pro-Fit' (pprofit) package [44] utilizing the Particle Swarm (as implemented in the Inspyred python library [45]) and a Nelder–Mead simplex to minimise the merit function.

DFT simulations were performed using CASTEP [46, 47] and employed the Generalised Gradient Approximation

Table 1. Partial charges assigned to ions in $YBa_2Cu_3O_7$.

Species	Charge (e)
Y	1.9
Ba	1.5
Cu	1.4
O	−1.3

(GGA) exchange correlation functional of Perdew *et al* [48]. Atoms were represented using a plane wave basis and ultrasoft pseudopotentials (generated using CASTEP's on-the-fly pseudopotential generator) with the plane wave expansion truncated at 600 eV. A high density Monkhorst–Pack [49] grid of $8 \times 8 \times 4$ *k*-points was used to sample the Brillouin zone. Energy minimisation of the unit cell resulted in lattice parameters of 3.820, 3.884 and 11.676 Å [50] compared to values of 3.839, 3.920 and 11.828 Å from experiment [51].

The potential is extended for use at higher temperatures by fitting to lattice parameters at 150, 300, 450 and 1100 K from *ab initio* molecular dynamics simulations (AIMD). AIMD simulations employed a $2 \times 2 \times 1$ supercell containing 62 atoms with a $2 \times 2 \times 2$ *k*-point grid used to sample the Brillouin Zone (this corresponds to a $4 \times 4 \times 2$ grid in the unit cell). The simulations were performed in the NPT ensemble with the temperature maintained using a Nosé–Hoover thermostat [52] and the pressure controlled with a Parrinello–Rahman barostat [53, 54]. To ensure computational tractability the planewave cutoff was reduced to 500 eV. The AIMD simulations employed a 1 fs timestep and lasted for 5 ps.

The classical molecular dynamics used during potential fitting used a supercell of $5 \times 5 \times 3$ unit cells to give a total of 975 atoms. The timestep used was 1 fs over 80 000 steps. The Nosé–Hoover barostat was employed with a relaxation time of 1 ps and the thermostat, had a time constant of 0.05 ps. An average of the lattice parameters was taken over the last 20 000 timesteps. A merit function was calculated from finding the difference in the potential and DFT parameters (the lattice parameters, elastic constants, phonon frequencies and bulk modulus) with various weighting factors applied. In order to ensure that the crystal structure was maintained during dynamics simulations the fractional co-ordinates were also included into the merit function (note that this constraint was relaxed for oxygen at higher temperatures to allow for diffusion).

Elastic constants were calculated using GULP, where the system was energy minimised using a Newton–Raphson optimiser, lower triangular hessian and Broyden–Fletcher–Goldfarb–Shanno (BFGS) algorithm [55]. GULP was also used to ensure that there were no negative phonon frequencies present when using the final potential.

As discussed above, the model must allow the exchange of Cu ions between the different sites without distorting the crystal structure. Therefore, the potential has been developed such that the charge on all Cu ions are the same. The charges on the Cu as well as the other ions are presented in table 1. The final Buckingham potential parameters for all pairwise interactions are given in table 2.

Table 2. Buckingham potential parameters for $YBa_2Cu_3O_7$.

Interaction	A (eV)	ρ (Å)	C (eV Å^6)
Ba–Ba	1781.39 851	0.36 211 849	0.41 044 8977
Y–Y	1586.26 765 436	0.33 160 7057 597	0.26 414 9391
Cu–Cu	4355.88 024 238	0.26 125 4935 725	0.09 804 4429
Ba–Y	1533.2020 975	0.39 191 5767 412	0.48 977 0321
Ba–Cu	516.28 511 2287	0.28 505 1454 016	0.20 082 6507
Y–Cu	2683.98 967 322	0.28 236 6684 384	0.47 088 7026
Ba–O	1814.69 835 133	0.32 864 4269 153	0.41 399 9523
Y–O	2113.25 500 501	0.28 605 4586 893	2.84 762 3285
Cu–O	2778.09 716 104	0.23 281 0703 093	0.11 892 4399
O–O	2079.31 685 441	0.23 810 897 103	49.97 870 249

Figure 2 shows the lattice constants at various temperatures from molecular dynamics simulations using the potential parameters presented in table 2 for $YBa_2Cu_3O_7$. Also plotted are the constants generated by DFT that formed the fitting database. The lattice parameters all increase with temperature smoothly and are a good fit to the DFT data. By comparison, the Chaplot potential gives reasonable agreement with the DFT for the *a* parameter, but not the *b*, where it is below the standard deviation of the DFT data.

Table 3 shows the elastic constants calculated using the new potential compared to values from the literature. As evident from table 3 the potential can reproduce the constants from DFT and experiment well, though in general the numbers are slightly lower. The bulk modulus predicted using the potential 93 GPa which is slightly lower than the 110 GPa from DFT.

3.3. Defect energies

Defect energies were calculated using the Mott–Littleton methodology [58] in the GULP code. Within this approach the lattice is partitioned into three concentric regions centred on the point defect of interest. As the presence of the defect is expected to result in a strong perturbation of the local crystal structure, in the central region, called Region I, ions are treated using the new empirical potential and the Cartesian co-ordinates are solved explicitly to achieve a force balance. The ions of region IIa are relaxed in one step using the Mott–Littleton approximation, which allows only harmonic displacements from their ideal positions, with the interactions between regions I and IIa calculated explicitly. Finally, the outermost region, IIb is an array of point charges and is used to represent the Madelung field of the infinite crystal. In this work, the radii for the Region I and Region IIa are 18 Å and 28 Å.

3.4. Oxygen diffusivity

The oxygen diffusivity was examined from molecular dynamics. Simulation supercells were constructed from $30 \times 30 \times 6$ replications of the $YBa_2Cu_3O_7$ unit cell and were then equilibrated for 2 ps under NPT conditions at the temperature of interest. Subsequently, the ensemble was switched to the microcanonical (NVE) ensemble and the mean squared displacement (MSD) of oxygen was recorded over

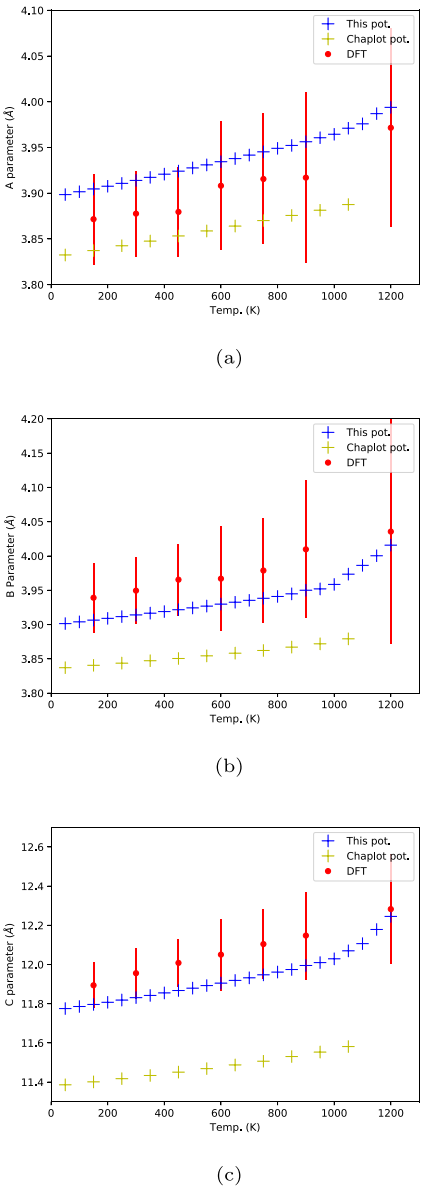

Figure 2. Lattice parameter a, b and c for $YBa_2Cu_3O_7$ with this potential (blue) taken every 50 K between 0 and 1200 K alongside the that of the Chaplot potential (yellow). DFT and its error bars in red.

50 ps. The diffusivity, D, can then be related to the MSD according to:

$$D = \lim_{t\to\infty} \frac{1}{2d} \frac{\left[\overrightarrow{r_i}(t) - \overrightarrow{r_i}(t_0)\right]}{t} \tag{5}$$

where, d is the dimensionality and t is the time [59]. The activation energy can then be extracted from an Arrhenius plot, where the natural log of the diffusivity is plotted against the inverse temperature.

3.5. Threshold displacement energies

The threshold displacement energy here is the energy it takes to displace an atom from its site to form a stable defect. This is different to the Frenkel and defect formation energies since it also requires the atoms to overcome the barrier to move away from their lattice sites. The threshold displacement energy is, therefore, directional since it will depend on the atom's local environment; this is especially true in $YBa_2Cu_3O_7$ because of its highly anisotropic structure.

Table 3. Elastic constants in fitting database in GPa. The matrix is diagonally symmetric such that $c_{12} = c_{21}$ and elements not tabulated (e.g. c_{41}) are not fitted. The experimental values come from [56, 57] and references therein.

Matrix element	DFT (GPa)	Potential (GPa)	Experiment (GPa)
c_{11}	215.97	166.45	211–234
c_{12}	109.24	73.23	37–132
c_{13}	58.03	42.65	70–100
c_{22}	232.40	180.30	230–268
c_{23}	57.16	52.62	93–100
c_{33}	142.56	163.76	138–186
c_{44}	51.19	48.82	35–61
c_{55}	41.19	28.51	33–50
c_{66}	81.73	69.85	57–97

To calculate the threshold displacement energies, a simulation supercell containing 3328 atoms was equilibrated at 25 K, then the velocity of a target atom was increased in the direction of interest. The MD simulation was then performed and the trajectory of the target atom was monitored for the formation of a defect. If no defect was detected the launch velocity, and hence kinetic energy, was increased until a defect was formed.

Ideally every direction would be tested multiple times to form a probability distribution as a function of direction around every atom site, as performed by Jackson *et al* [60]. However, here to provide an initial exploration of the directional dependence of the damage process, we consider a selection of directions (specifically x, y, z, xy, xz and yz) for each unique site.

3.6. Radiation damage cascades

3.6.1. Cascade simulations. In order to simulate neutron damage, we employ the primary knock-on atom (pka) methodology. Within the pka method the velocity of a single atom is rescaled to represent the transfer of kinetic energy from the projectile. In this study we rescale the velocity of Ba atoms after which the system was allowed to evolve in response to the transfer of energy to the pka. According to the Kinchin–Pease [61] and Norgett–Robinson–Torrens (NRT) [62] models the number of defects created during a cascade is related to the threshold displacement energy of the pka, therefore, it is anticipated that O and Cu pkas would result in more defects being created than seen here, while a Y pka would result in roughly the same number of defects. However, we leave a detailed exploration of the impact of the choice of pka to future work.

The size of supercells considered here was large enough for the applied pka energy to avoid the cascade reaching the cell boundary, which as described below is thermostated. This necessitates larger boxes for higher energy cascades, in this case a one million atom supercell was used for the 5 keV pkas

up to a 10.5 million atom cell for the 20 keV pkas. Changing the size of the simulation supercell introduces a change in the effective fluence being studied. At the fluences expected in a reactor it is anticipated that cascades will occur in regions that have already been damaged. The impact of these overlapping cascades can also be studied using MD enabling an extrapolation to the fluence of interest [63]. He simulation cells were initially equilibrated under NPT conditions at the temperature of interest for 80 000 timesteps. The equilibrated supercells were then used as the starting systems for the cascade simulation. In order to examine the dependence of initial pka direction on defect creation, three different crystallographic directions were considered for the cascades.

During the cascade simulations, the central region of the simulation supercell adopted the microcanonical (NVE) ensemble. In order to represent heat diffusion away from the cascade, a velocity rescaling thermostat is used in the outer layer of 10% of the width around the supercell, isolating a spherical non-boundary region where the cascade takes place. This thermostat had a relaxation period of 10 ps. At the end of the simulation, the average temperature of the entire system had returned to the equilibrated value.

The cascade simulations were performed using a variable timestep through the cascade propagation. At the initial stages of the cascades, a short timestep was used due to the high velocities of the pka and other atoms during the ballistic phase of the process. As the kinetic energy of displaced atoms is transferred to other atoms and thus dissipated in the system, the velocity of the atoms goes down, and the time step was increased. The variable timestep varied between 1.0×10^{-5} ps and 0.001 ps. The maximum allowed distance for atoms to move in one timestep was 0.1 Å. The cascade simulations were performed up to 120 ps to confirm a steady state in the production of defects.

3.6.2. Defect detection. Key to understanding how radiation damage will impact the evolution of the superconducting properties of $YBa_2Cu_3O_7$ during operation is understanding how the defect population changes. Therefore, it is essential to be able to accurately determine the number of defects produced as well as their types and distributions.

In simple structures, the number of defects is relatively easy to count, however, $YBa_2Cu_3O_7$'s complex crystal structure makes this a challenge for this material. Defect counting here was done using two different techniques. The first is the Wigner–Seitz (WS) method implemented in OVITO [64]. This method uses the final frame from the equilibration simulation as a reference 'defect-free' frame which is then subdivided into Voronoi cells. Interstitial, vacancy and antisite defects can be identified in any given subsequent frame by counting the number of atoms present in each Voronoi cell.

The second method, involves folding positions of the atoms in the supercell back down to the unit cell. Atoms that are not on their initial state are immediately obvious since they appear in-between sites. A *k*-means clustering algorithm has been trained to recognise each of the 43 sites that atoms commonly occupied (the 39 atom sites and the 4 identical interstitial 2 (in the $YBa_2Cu_3O_8$ regime) sites according to figure 3). The k-means algorithm was chosen over other clustering algorithms because it seeks to classify by distance, in keeping with an atomic structure, as opposed to classification by density, which would be problematic if sites are not densely populated. The algorithm is trained on either a folded supercell that was held at 360 K (at which temperature atoms populate all sites) for 120 ps, or on a unit cell where the sites have all been equally populated.

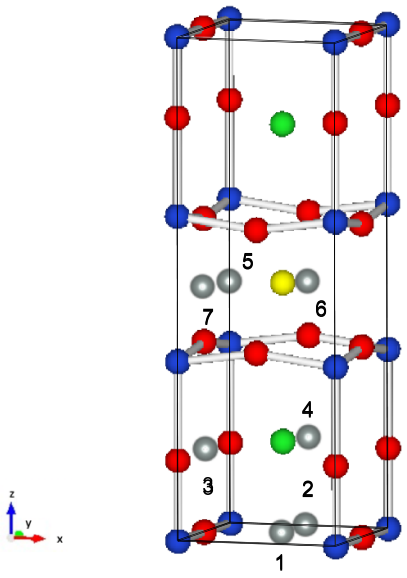

Figure 3. Graphical representation of the $YBa_2Cu_3O_7$ unit cell with the interstitial sites illustrated by the grey spheres. Red, blue, green and yellow spheres corresponds to oxygen, copper, barium and yttrium respectively.

The algorithm is able to assign a distinct label to each site. By comparing the initial population/unit cell to the folded supercells through the cascade, vacancies and interstitials can be easily identified. A weakness of the approach is that the algorithm will try to assign sites to all atoms, meaning that the 'true' populations of defects will be covered in statistical noise of the atoms that are in between sites (i.e. are amorphous). This is the same weakness as any defect classifier will have, and is present in the WS method described above. Overall trends in defect counts are still visible. Its advantage over the WS method is that it is possible to quickly detect common features in defect formations, in particular a new interstitial site, leaving vacancies in the Cu–O chain and plane sites.

4. Results and discussion

Aside from the properties included in the fitting database, additional properties of the potential should be calculated and compared to existing values for the physical properties of $YBa_2Cu_3O_7$ to establish the predictive ability of the model.

Table 4. Defect energies calculated using the potential compared to defect formation energies determined from DFT for vacancy defects in $YBa_2Cu_3O_7$ (note reported DFT energies correspond to the rich state). The positions of the different lattice sites can be established from figure 1.

Vacancy site	DFT (eV)	Potential (eV)
Y	10.8	22.00
Ba	7.17	9.76
Cu1	2.15	15.12
Cu2	1.76	13.45
O1	1.01	10.30
O2	1.6	9.45
O3	1.71	9.38
O4	0.88	10.34

Table 5. Defect energies calculated using the potential compared to defect formation energies determined from DFT for interstitial defects in $YBa_2Cu_3O_7$ (note reported DFT energies correspond to the rich state). The positions of the different interstitial sites can be established from figure 3.

	O (eV)		Y (eV)		Ba (eV)		Cu (eV)	
Site	DFT	Potential	DFT	Potential	DFT	Potential	DFT	Potential
1	2.14	−6.74	−0.31	−6.17	1.84	0.03	1.52	−6.20
2	0.26	−8.42	−1.94	−7.62	0.55	−0.57	2.6	−5.18
3	2.27	−1.57	−1.61	−7.27	2.73	2.10	1.33	−7.53
4	0.27	−3.34	−1.31	−5.34	0.55	−0.57	1.81	−6.68
5	0.11	−5.51	−1.63	−10.70	3.06	0.99		−7.88
6	0.10	−1.15	1.65	−8.57	3.89	2.14	2.49	−6.05
7	0.11	−0.99	3.01	−7.62	5.55	3.03	3.27	−5.71

4.1. Defect energies and defect processes

It is the introduction of defects due to radiation damage that will ultimately cause the degradation of the superconducting properties of the $YBa_2Cu_3O_7$ during operation. Therefore, it is important to understand how the potential describes the point defects.

Given the difficulty in calculating defect energies experimentally the defect energies are compared to previous DFT data [50]. Comparison of defect formation energies determined from DFT and defect energies from empirical potentials is non-trivial due to the inclusion of the internal energy in the DFT energies and its absence in the classical models. This makes comparisons of the absolute energies difficult, although it can be useful for comparing defects of the same type. This situation is significantly more complicated for $YBa_2Cu_3O_7$ due to the handling of the charges in the different simulations. As a ceramic oxide $YBa_2Cu_3O_7$ consists of charged ions. Within the potential model, therefore, a vacancy defect is created by removing an ion resulting in a charged defect. By contrast, in the DFT simulations when defects are introduced the simulation supercells are charge neutral as any electrons added/removed would be added or removed from the electron reservoir which will remain essentially fixed. Therefore, there is no direct equivalence between the two. Nevertheless, an examination of the defect chemistry predicted by the potential is useful for understanding the structural evolution during the cascades.

Table 4 shows the defect energies for the vacancy defects in $YBa_2Cu_3O_7$ compared to the DFT values. The key observation from table 4 is that the potential predicts that the oxygen vacancy prefers to reside in the CuO_2 planes rather than in the chains or on the apical (O4) site as generally anticipated [65] and predicted using DFT [50, 66]. This reversal of the observed preference for the oxygen vacancy is also observed if the Chaplot potential is used with all oxygen ions treated equivalently. The Baetzold potential is only able to overcome this shortcoming by using different charges on the ions on the two Cu sites. The origin of this discrepancy is the difference in Madelung potentials for the two sites. Therefore, the Coulombic energy difference between the two sites cannot be compensated if the same potentials are present. While this may appear to be a significant limitation of the potential it does not seem to influence the overall picture observed during the cascades as will be discussed later. For the copper ions the potential predicts that the Cu2 site is the most favourable site for the vacancy in agreement with the DFT simulations.

The next defects we examine are the interstitial defects in $YBa_2Cu_3O_7$, for which the defect energies are presented in table 5. Given the complex crystal structure there are a large number of possible interstitial sites examined and these are illustrated in figure 3. For the Ba interstitial defects there is good agreement between the potential and the DFT as both techniques predict that the interstitial 2 site is the most favourable and that the 4 site is unstable as the Ba ion relaxes onto the 2 site. The 2 site is also predicted to be the most thermodynamically stable interstitial site for oxygen, which is in contrast to the DFT that predicts that the interstitial site number 5 is most stable. However, many crystallographic studies

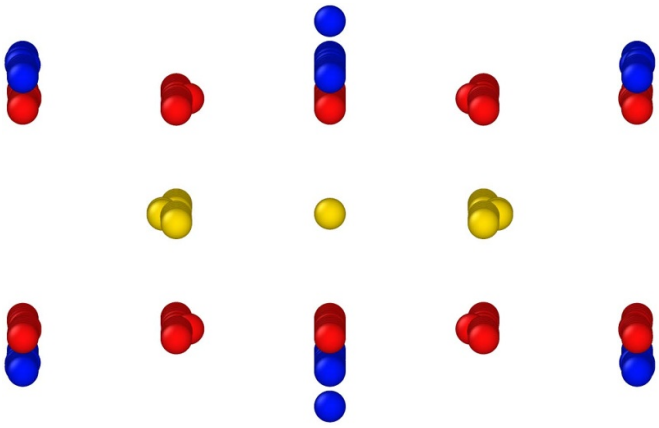

Figure 4. Example split interstitial structure shown in the x–z plane. A Y atom inserted into interstitial site 5 has caused the neighbouring Cu atoms to form a split interstitial. O in red, Y in yellow and Cu in blue.

Table 6. Defect energies calculated using the potential compared to defect formation energies determined from DFT for antisite defects in $YBa_2Cu_3O_7$ (note reported DFT energies correspond to the rich state). The positions of the different lattice sites can be established from figure 1.

Defect	DFT (eV)	Potential (eV)
Ba_Y	4.34	10.82
Y_{Ba}	−2.81	−8.74
Ba_{Cu1}	−1.56	9.08
Ba_{Cu2}	−0.63	7.28
Cu_{Ba}	5.7	−2.75
Cu_Y	9.55	6.28
Y_{Cu1}	−4.97	−2.96
Y_{Cu2}	−6.17	−2.36

of $YBa_2Cu_3O_7$ suggest that the interstitial site 2 is partially occupied by oxygen, while there is no evidence of significant quantities of oxygen residing in the Y layer. For both the Cu and Y ions the interstitial 5 site is found to be the most energetically stable. This site may not seem particularly attractive for the cations to reside in, however, they are able to displace neighbouring Cu ions to create a complex split interstitial defect as illustrated in figure 4. The DFT simulations were performed in a $4 \times 4 \times 1$ supercell that may not be sufficiently large to allow the level of distortion predicted by the potential and this should be examined in future work.

The final class of defects examined are the antisite defects, for which defect energies are presented in table 6. The results show that the potential predicts that Y prefers to sit on the Cu1 site while Ba favours the Cu2 site with both of these being opposite to what is predicted by DFT.

Based on the defect energies it is possible to determine the reaction energies for the intrinsic defect processes and these are presented in table 7. Table 7 shows that the defect chemistry predicted by the potential is similar to that predicted using DFT with both predicting the dominance of the oxygen Frenkel process and the Y/Ba antisite reaction. This is then followed by the remaining cation antisite processes with the

Table 7. Frenkel defect formation energies per species.

Species	DFT (eV)	Potential (eV)
Y Frenkel	4.46	5.65
Ba Frenkel	3.86	4.59
Cu Frenkl	3.08	2.79
O Frenkl	0.49	0.48
Y/Ba antisite	0.76	1.04
Ba/Cu antisite	1.69	2.27
Y/Cu antisite	2.07	2.16

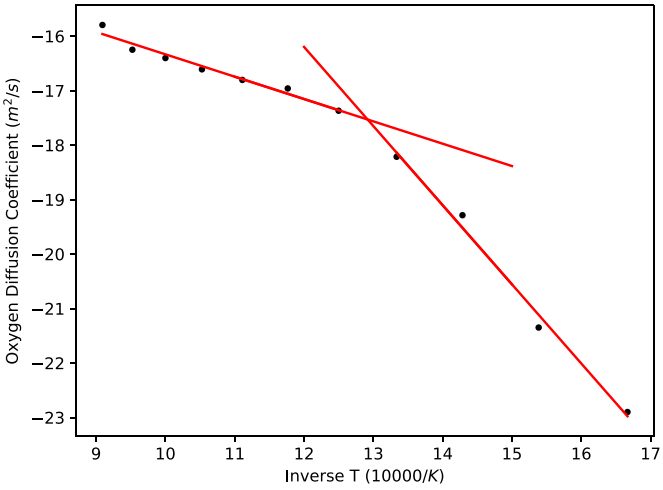

Figure 5. Arrhenius plot showing the diffusivity of oxygen as a function of 1/T. From the two gradients activation energies of 1.19 and 0.4 eV were determined.

cation Frenkel processes, with the Y Frenkel process exhibiting the highest energy. Overall the potential demonstrates reasonable agreement with the DFT simulations despite the very complex defect chemistry present in the material.

4.2. Oxygen diffusivity

Using the MSDs from simulations in the temperature range 600–1100 K it is possible to create an Arrhenius plot which is presented in figure 5. There are two regimes in the data, with a transition at around 850 K. This indicates there are two diffusion mechanisms occurring. The two gradients correspond to activation energies of 1.19 eV (at $T < 850$ K) and 0.4 eV (850 K–1100 K). This compares to values in the range 0.9–1.2 eV [67–69] found experimentally. While this activation energy may be below the experimental energy in one regime, largely it is an improvement of a value of 0.52 eV obtained using the Chaplot potential when implemented as found in [35].

4.3. Threshold displacement energy

The threshold displacement energies for all of the symmetrically distinct sites are presented in table 8. The threshold displacement energies for oxygen are typically in the region 9-26 eV although the values can be as low as 2.5 eV for the O4 atom in the xz direction or as high as 67.34 eV for the O2

Table 8. Threshold displacement energies for each site type and direction in eV.

	x	*y*	*z*	*xy*	*xz*	*yz*
O1	9.141	12.95	15.11	17.43	19.92	15.11
O2	12.95	25.39	12.95	25.39	15.11	67.34
O3	15.11	12.95	12.95	17.43	25.39	17.43
O4	15.11	17.43	38.32	15.11	2.5	22.57
Cu1	9.961	9.961	23.79	13.91	6.668	
Cu2	9.961	29.72	29.72	36.31	9.961	13.91
Ba	78.46	30.07	51.42	4.45	51.42	30.07
Y	33.287	33.287	50.794	33.287	41.58	41.58

atom in the *yz* direction. Given the stochastic nature of the threshold displacement energies these values should be considered atypical. These values agree well with previous values determined using the modified Chaplot potential [6, 25, 33] of 4.2–18.8 eV. The average O atom threshold displacement energy is 16.8 eV.

The displacement energies for the Cu sites are between 6.67 eV and 29.72 eV. It has been noted previously that it is easier to displace ions from the CuO chain than in the CuO_2 plane [70, 71]. This is reflected in the relatively low energies for displacement from the O1 and Cu1 sites. The Ba and Y sites have much higher threshold displacement energies, as expected for larger cations.

4.4. Cascades

We begin our discussion of the radiation damage cascades by presenting some snapshots of a cascade resulting from a Ba pka with an energy of 5 keV at a temperature of 25 K. Figure 6 shows some general features of the cascades and allows us to highlight some important points. In general, the cascades result in disordered regions consisting of defects of all types, surrounded by a region consisting predominantly of Cu and O defects.

The highly disordered regions resemble those seen in experimental observations of radiation damaged $YBa_2Cu_3O_7$ [72]. The extent of the disordered region can be estimated by constructing a surface mesh around the defect cluster and a volume can be extracted. An example of a cascade with the surface mesh applied over the amorphous region is presented in figure 7.

Outside of the amorphous regions there is a peripheral region dominated by Cu and O defects that occur predominantly in the CuO-chains. An example is illustrated in figure 8. It is clear that the defects created are organised into planes. This will be discussed in more detail later on.

Also evident from figure 6 is the relatively low level of recombination that occurs during the cascade. To illustrate this, the peak and final vacancy counts for 5 keV Ba pkas are presented in table 9. These cascades all take place at 25 K which is the proposed operating temperature of the magnets in a reactor. We have shown two cascades in the *x* direction to demonstrate the stochastic nature of defect creation and recombination, as well as cascades in each of the *y* and *z* directions to demonstrate the effect of the anisotropic crystal structure.

Table 9 shows that there is between 30% and 50% recombination, which is much lower than expected in materials that are considered radiation tolerant, such as UO_2 [22, 73].

Using the Wigner–Seitz analysis it is possible to qualitatively determine the types of defects being formed during the cascade. Figure 9 shows that the total number of vacancies of each type as a function of time resulting from a 5 keV Ba pka at 25 K averaged over 15 simulations. The plot shows that the number of oxygen vacancies created during the cascade is significantly greater than the cation vacancies. This is in agreement with the lower threshold displacement energies discussed earlier. Further the fraction of oxygen vacancies that undergo recombination is significantly smaller than is the case for the cations.

To explore the directional dependence of the cascade on vacancy creation a series of nine cascades were performed in each Cartesian direction. The resulting average vacancy concentrations are presented in figure 10. There appears to be a slight directional dependence in the number of O, Ba and Y vacancies remaining at the end of the cascade. There is a greater directional dependence on the peak number of defects produced and this is apparent for all the different ion types although is most pronounced for the Cu vacancies with more produced for pkas launched in the *z* direction, than in the *x* and *y* directions. There tends to be slightly more variation in cascades started in the *x* direction for all atom types.

The next defect types examined are antisites, for which the results are shown in figure 11. The most common anitsites are the Cu_{Ba} defects followed by roughly equal numbers of Ba_{Cu} and Cu_Y, defects. The Y_{Cu} defects are produced in the smallest numbers during the cascade. It is noted that the standard deviation in the number of Cu_{Ba} defects across the 15 cascades is more significant than for the other antisites.

Thus far, only cascades of 5 keV have been considered, therefore, we now examine how the total number of defects changes as a function of the pka energy. As illustrated in figure 12, there is a linear increase in the number of defects produced as the pka energy increases, a trend that has been observed elsewhere [74, 75]. Of particular importance in HTS materials is the volume of the disordered region, as these can act as flux pinning centres. As discussed above, the volume of the amorphous region can be estimated by constructing a surface mesh that encloses the amorphous region. The change in the volume of the disordered region as a function of energy is presented in figure 13.

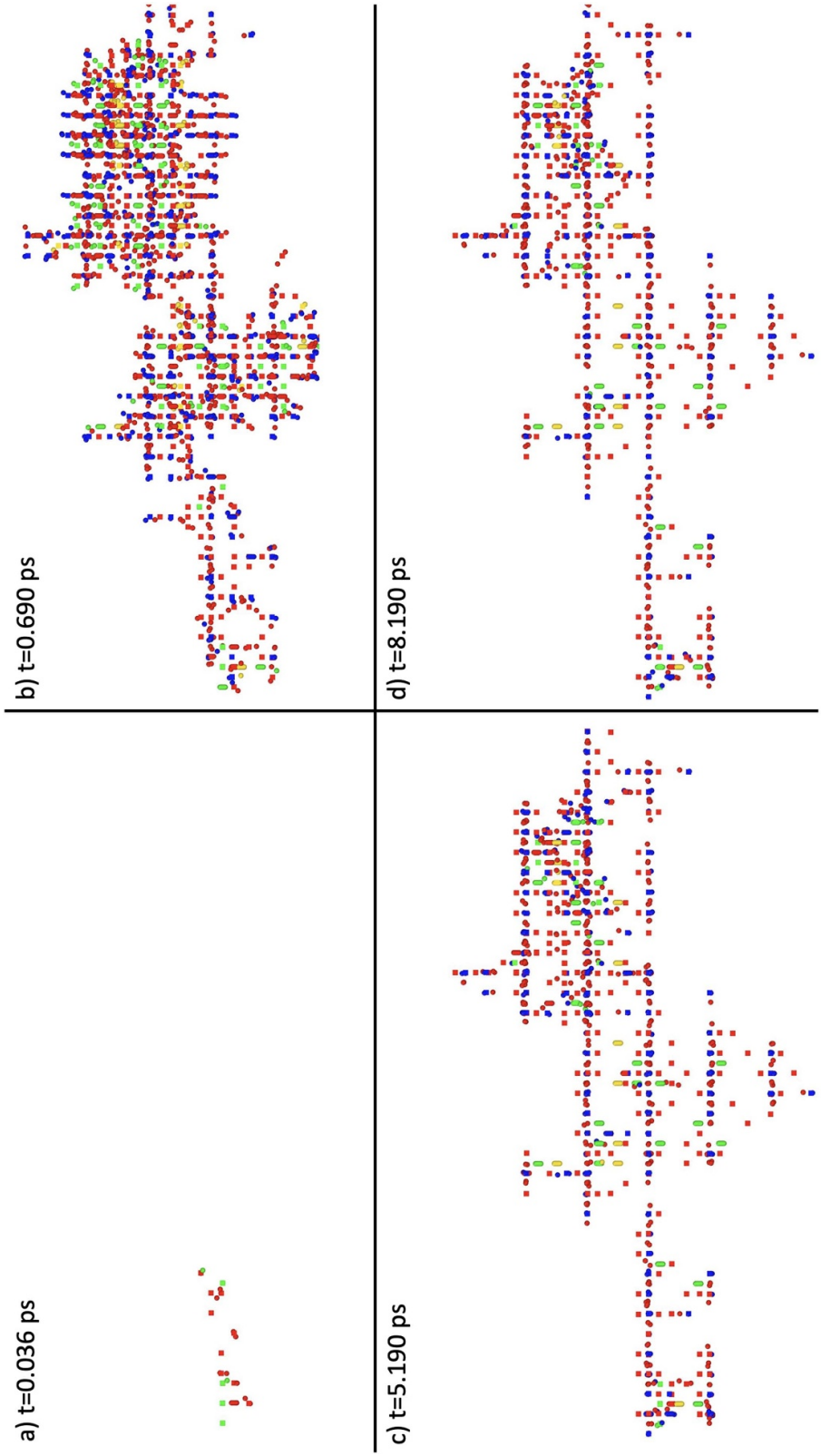

Figure 6. Four images in the x–z plane of the cascade progression of a 5 keV 25 K cascade with pka launched in the x direction taken at the beginning, peak damage, recombination and final state. Vacancies are cubes, interstitial are spheres, antisites are spherocylinders colored by the host site as in figure 7.

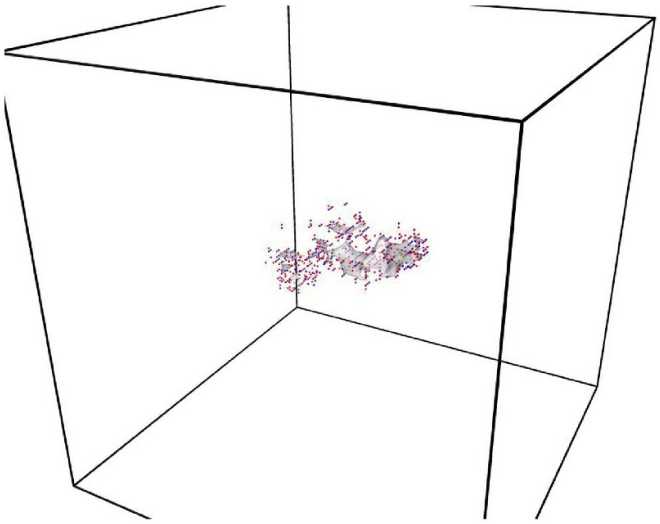

Figure 7. Final frame of cascade X-1, 5 keV Ba pka at 25 K in the x direction in $YBa_2Cu_3O_7$, with overlayed surface mesh. Colour coded with O as red, Ba as green, Y as yellow and Cu as blue.

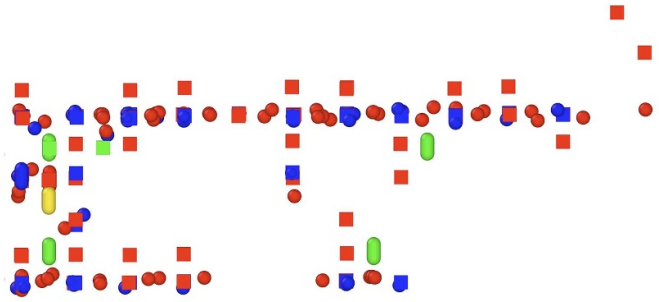

Figure 8. An image showing the periphery of a cascade showing the Cu and O defects in the same cascade as in figure 6. The cascade was a 5 keV cascade with a pka launched in the x direction, with this image taken at 5.19 ps. Vacancies are cubes, interstitial are spheres, antisites are spherocylinders colored by the host site as in figure 7.

Table 9. For a selection of cascades at 5 keV and with a Ba PKA at 25 K, the peak vacancies, final vacancies, and % recombination.

Cascade identifier	Peak vacancies	Final vacancies	% recombination
X-1	587	330	44%
X-2	636	325	49%
Y-1	502	340	32%
Z-1	462	300	35%

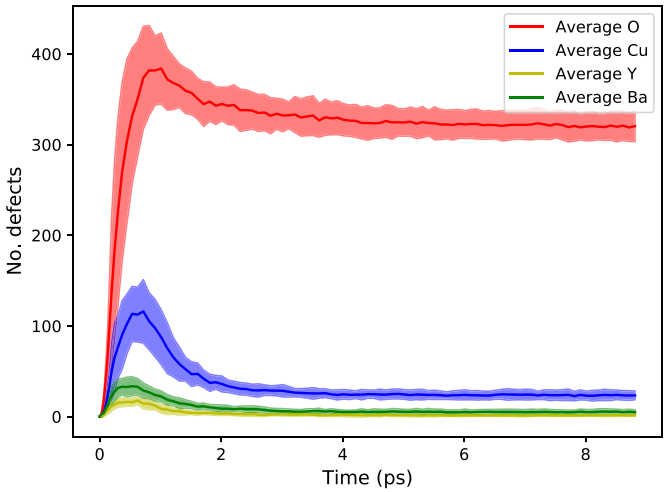

Figure 9. Time evolution of number of vacancies per type produced on average of 15 cascades with their standard deviations in the shaded regions at 25 K.

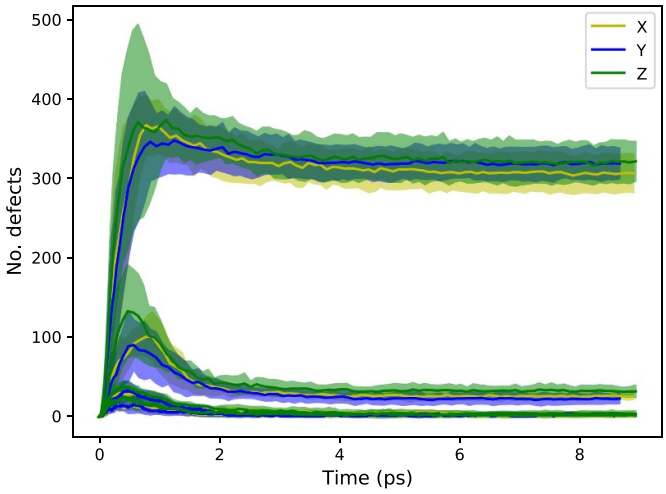

Figure 10. Time evolution of number of vacancies produced on average of nine cascades per direction with their standard deviations in the shaded regions at 25 K. All types of atoms are show, giving the graph the same bands of plot lines as in figure 9. In this plot, the different colors represent the initial PKA direction. Therefore, since in each band the standard deviation of the directions overlap, we conclude there is no strong directional dependence of the number of defects produced on a per atom type basis.

If the relationships between cascade pka energy and number of defects or volume of amorphous region hold as the cascade energy increases, this analysis may hold the power to predict defect volume in the material. Experimental results [10] have shown an initial increase in critical current J_c but then a decrease as damage increases. A predictive relationship between the volume of the amorphous region and the energy of a cascade might help explain these results. Further, as this potential is used at higher energies similar to those on experimental scales, the damage processes may be better understood as the predicted structures and experimental results are compared.

The overall morphology of the remnant defects is similar at the higher energies. An example of a 20 keV Ba pka is presented in figure 14. The cascade presented in figure 14 shows evidence of some cascade branching. These branches form smaller cascades, comparable in size to those observed at 5 keV, each with the common amorphous core and surrounding damage, mostly in the CuO-chains. These amorphous cores are visible as the smaller meshed regions in the left, bottom and top right of the image. At the end of the cascade it appears that there are

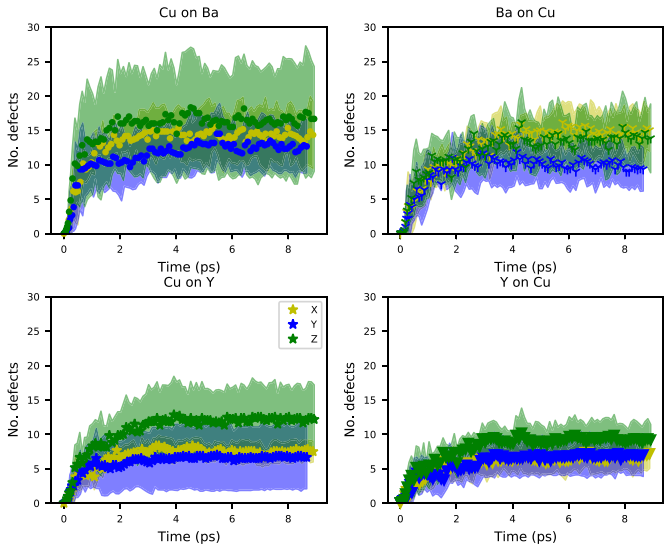

Figure 11. Quadrant plots showing the evolution of number of antisites for the dominant cation processes produced on average of nine cascades per direction with their standard deviations in the shaded regions at 25 K. They share axes for direct comparison, labelled on the Cu on Y plot. Since the standard deviation in the number of defects for all directions tend to overlap, we conclude there is little directional dependence in cation antisite defect creation.

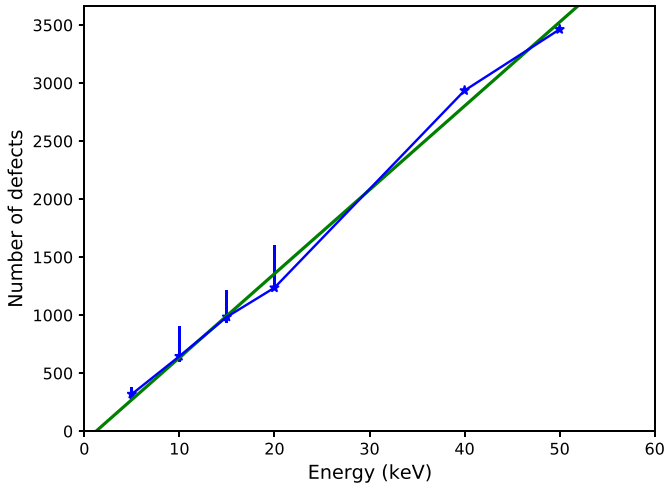

Figure 12. Time evolution of number of vacancies produced with increasing pka energies. Deviance from the straight line relationship is shown.

small amorphous regions connected by regions rich in Cu and O defects. The total amount of amorphous region does increase with pka energy, but it is important to note that this is likely the result of multiple smaller amorphous cores.

As discussed above, the majority of defects are to be found in the disordered region, however, there are also Cu and O defects in the peripheral region. At first glance it appears there are oxygen interstitial defects around the CuO chains which must be balanced by O vacancies elsewhere in the crystal. This phenomena can be explored more closely using the folding method of defect detection. An example of a snapshot

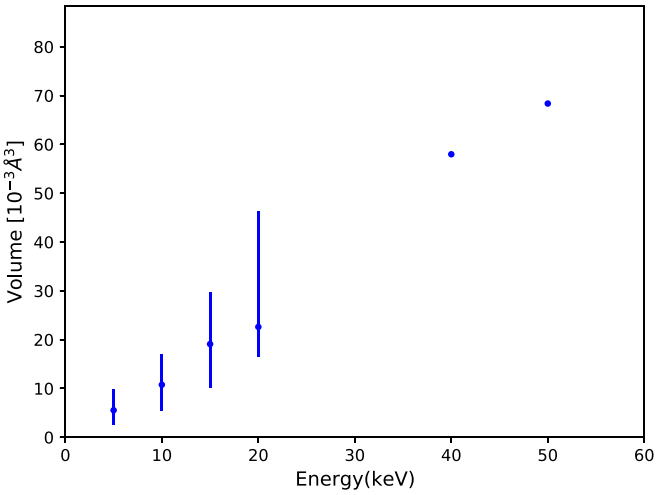

Figure 13. Time evolution of size of the amorphous region produced in the cascade with increasing pka energies.

from a cascade involving a 5 keV pka at 25 K is illustrated in figure 15. The figure shows that there are large concentrations of spheres present in the regions corresponding to the lattice sites with some variation due the temperature deposited into the lattice by the pka. In addition there are atoms distributed randomly throughout the cell and these are either contained in the amorphous region or interstitial defects on the periphery. What is particularly interesting, is the accumulation of oxygen ions in the interstitial 2 site in the Cu–O chains illustrated in figure 15.

As the location of oxygen vacancy defects is thought to have a strong impact on the superconducting properties of $YBa_2Cu_3O_7$ it is essential to understand where these oxygen ions that now occupy the interstitial 2 site come from. To understand this the number of vacancy defects on each of the four unique oxygen sites is presented in figures 16(b) and (d) for 25 K and 360 K respectively.

The contribution to the interstitial 2 site (i.e. how many oxygen ions occupied the site prior to the cascade beginning) is also included in figures 16(b) and (d). The population is 0 in the 25 K case, showing there is no underlying population. At 360 K there is already a small number of oxygen ions residing on the interstitial 2 site, this is due to the fact that oxygen is already able to diffuse at this temperature. Both figures 16(b) and (d) show that the majority of oxygen ions moving to populate the interstitial 2 sites come from the O1 and O4 sites. These are the chain sites, as opposed to the plane sites, O2 and O3 which only contribute 4% at 25 K and 3% at 360 K. We further examine the temperature dependence in figure 16 panels (b) and (d).

The difference in percentage contribution with temperature stems from the fact that there are more ions moving from the O1 and O4 sites into the interstitial 2 site than from the O2 and O3 sites as illustrated in figures 16(b) and (d). Therefore, the results indicate that the cascade leads to the displacement of oxygen ions from the O1 and O4 sites into the interstitial 2 site, and that this effect is greater at high temperature. This is despite the potential favouring vacancy formation on the plane

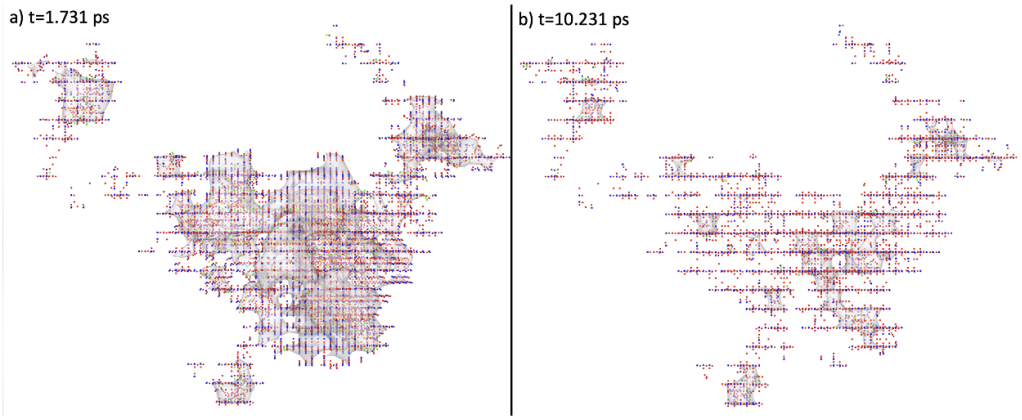

Figure 14. Two images of the cascade progression in the x–z plane of a 20 keV cascade with pka launched in the x direction taken at the peak damage and final state. Vacancies are cubes, interstitial are spheres, antisites are spherocylinders colored by the host site as in figure 7.

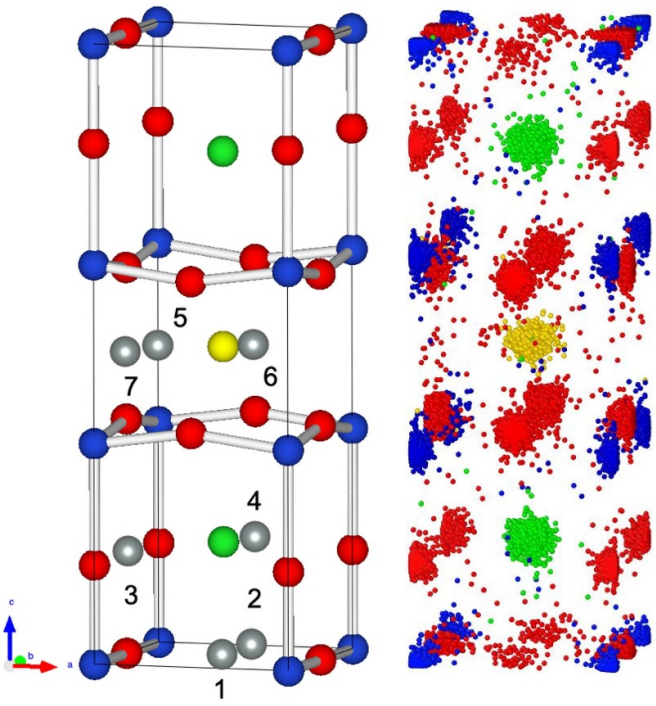

Figure 15. (Left) The unit cell schematic from figure 3 alongside (right) an image of a 25 K $YBa_2Cu_3O_7$ supercell folded down to its unit cell at 5.4 ps (toward the end of the recombination phase). During the cascade, the interstitial 2 sites have been populated with Oxygen interstitials (red).

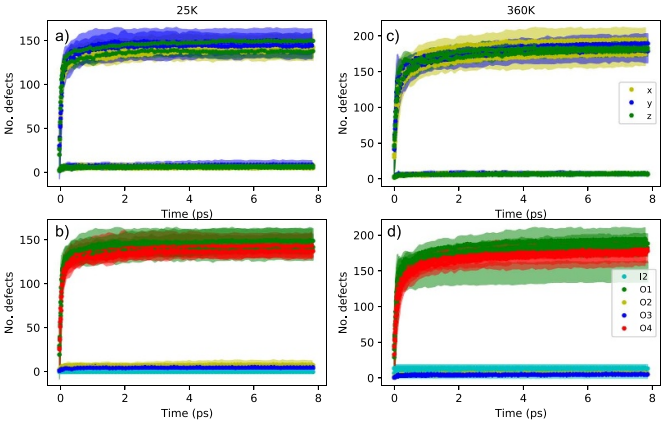

Figure 16. A quadrant plot showing the time evolution of the number of atoms on interstitial site 2. Both panels of the left hand site are at 25 K and the right hand side are at 360 K.The same data is being shown within the left and right hand sides with different colour coding to demonstrate different features of the plots. The bottom panels are color coded according to their origin site, whereas the upper panels are color coded according to the launch direction of the incoming PKA. Each of the 15 sets of data per temperature are shown with the standard deviations in the shaded regions at 25 K (blue) and 360 K (red). These share axes for direct comparison, labelled in (b).

sites as discussed previously. Oxygen ions displaced from the plane sites are largely confined to the amorphous regions.

Examination of figures 16(a) and (c) shows that there is a small dependence on the direction of the pka and this appears to be slightly greater at the higher temperature.

Finally, we explore the impact of temperature by examining the number of defects created during cascades at the predicted operation temperature of 25 K and the temperature where existing experimental observations were performed. Presented in figure 17 is the average number of vacancies as a function of time for 15 pkas in the x direction. Clearly evident from figure 17 is that there is an increased number of defects created in the higher temperature cascade, and a concomitant higher number of defects at the peak. The peak also occurs slightly later in time than is the case at 25 K. This can be explained due to the increased volume of $YBa_2Cu_3O_7$ due to thermal expansion, offering more space between atoms making it easier to displace them. The level of recombination at the higher temperature, while greater than observed at the lower temperature, is not sufficient to drive the final number of defects lower. Ultimately, this is due to the formation of an amorphous region, where there is very little recombination.

As discussed in the introduction the study of Iliffe *et al* [11] suggests a similar decrease in the J_c and T_c at both room and operational temperatures. Further, when the low temperature irradiated samples were annealed at room temperature,

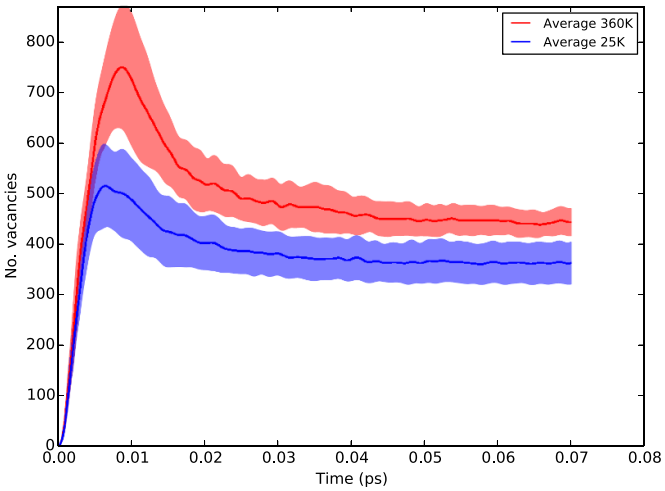

Figure 17. Time evolution of number of vacancies produced on average of 15 cascades with their standard deviations in the shaded regions at 25 K (blue) and 360 K (red).

there was some recovery of the superconducting properties. Figure 17 indicates that while there are fewer defects created at the lower temperature the difference is relatively modest. More interestingly, assuming the much lower number of defects created during the ballistic phase at 25 K was then subjected to annealing at room temperature resulting in a similar level of recombination as predicted at 360 K then the number of remnant defects will be significantly lower than if the irradiation itself had been performed at high temperature. This reduction in remnant defects would result in less degradation of the superconducting properties, therefore, the simulations appear to support the experimental observations of Iliffe *et al* [11].

5. Summary

Molecular dynamics simulations have been performed to determine the differences in radiation cascade defect production under expected operational conditions and those present during previous experimental studies. In order to enable these simulations a new empirical potential model for $YBa_2Cu_3O_7$ has been developed. This new potential allows the exchange of ions between the different copper sites with no adverse implications for the crystal structure. The potential is also shown to provide a good description of the defect chemistry of this complex material. Further the activation energy for oxygen diffusion is also found to be in close agreement with experiment.

The pka simulations suggest that the cascades result in the formation of amorphous regions that are surrounded by a periphery where there is a high population of defects in the CuO chains. The origin of this is the relatively low threshold displacement energies for ions in the chains and the presence of the relatively stable interstitial 2 site. By contrast, the population of oxygen vacancies in the planes appears to be relatively low with only a small number of these ions able to reach the stable interstitial 2 site. Introduction of small amorphous regions that can act as flux pinning centres and oxygen vacancies into the CuO planes may explain the observed increase in the superconducting properties, however, the long term accumulation of defects in the CuO_2 planes may cause the degradation observed at higher fluences.

The number of defects formed at the operational temperature of 25 K is predicted to be lower than observed at 360 K. This is due to creation of more defects during the ballistic phase coupled with inefficient recombination during the annealing phase at the higher temperature. The types of defects formed and their distributions predicted at the two temperatures are also found to be similar.

Data availability statement

The data that support the findings of this study are available upon reasonable request from the authors.

Acknowledgments

Funding for this work was provided by Tokamak Energy and EPSRC (EP/R511560/1). Via our membership of the UK's HEC Materials Chemistry Consortium, which is funded by EPSRC (EP/L000202, EP/R029431), this work used the ARCHER UK National Supercomputing Service (www.archer.ac.uk).

ORCID iDs

M J D Rushton https://orcid.org/0000-0001-7650-4377
S T Murphy https://orcid.org/0000-0001-7605-9613

References

[1] Lawson J D 1957 Some criteria for a power producing thermonuclear reactor *Proc. Phys. Soc.* B **70** 6–10
[2] Gryaznevich M and Sykes A 2017 Merging-compression formation of high temperature tokamak plasma *Nucl. Fusion* **57** 072003
[3] Sykes A *et al* 2014 Recent advances on the spherical tokamak route to fusion power *IEEE Trans. Plasma Sci.* **42** 482–8
[4] Costley A, Hugill J and Buxton P 2015 On the power and size of tokamak fusion pilot plants and reactors *Nucl. Fusion* **55** 033001
[5] Sykes A *et al* 2018 Compact fusion energy based on the spherical tokamak *Nucl. Fusion* **58** 016039
[6] Cui F, Li H, Jin L and Li Y 1994 Simulations on radiation damage initiated by O(1) pka in $YBa_2Cu_3O_7$ *Nucl. Instrum. Methods Phys. Res.* B **91** 374–7
[7] Cannelli G, Cantelli R, Cordero F, Ferretti M and Trequattrini F 1991 Fast oxygen mobility in tetragonal $YBa_2Cu_3O_{7-x}$ by anelastic relaxation measurements *Solid State Commun.* **77** 429–31
[8] Sauerzopf F, Wiesinger H, Kritscha W, Weber H, Crabtree G and Liu J 1991 Neutron-irradiation effects on critical current densities in single-crystalline $YBa_2Cu_3O_{7-\delta}$ *Phys. Rev.* B **43** 3091
[9] Chudy M, Eisterer M, Weber H, Veterníková J, Sojak S and Slugeň V 2012 Point defects in $YBa_2Cu_3O_{7-x}$ studied using positron annihilation *Supercond. Sci. Technol.* **25** 075017

[10] Fischer D, Prokopec R, Emhofer J and Eisterer M 2018 The effect of fast neutron irradiation on the superconducting properties of REBCO coated conductors with and without artificial pinning centers *Supercond. Sci. Technol.* **31** 044006

[11] Iliffe W, Peng N, Brittles G, Bateman R, Webb R, Grovenor C and Speller S 2021 *In-situ* measurements of the effect of radiation damage on the superconducting properties of coated conductors *Supercond. Sci. Technol.* **34** 09LT01

[12] Pedarnig J, Bodea M, Steiger B, Markowitsch W and Lang W 2012 Systematic modification of electrical and superconducting properties of YBCO and nano-patterning of high-T_c superconducting thin films by light-ion irradiation *Phys. Proc.* **36** 508–13

[13] Huang D, Gu H, Shang H, Li T, Xie B, Zou Q, Chen D, Kan Chu W and Ding F 2021 Enhancement in the critical current density of $BaTiO_3$-doped YBCO films by low-energy (60 keV) proton irradiation *Supercond. Sci. Technol.* **34** 045001

[14] Roas B, Hensel B, Saemann-Ischenko G and Schultz L 1989 Irradiation-induced enhancement of the critical current density of epitaxial $YBa_2Cu_3O_{7-x}$ thin films *Appl. Phys. Lett.* **54** 1051–3

[15] Kumar R, Samanta S, Arora S, Gupta A, Kanjilal D, Pinto R and Narlikar A 1998 Study of columnar amorphization and structural symmetry changes produced by swift heavy ion irradiation in $YBa_2Cu_3O_{7-y}$ thin films using STM *Solid State Commun.* **106** 805–10

[16] Watanabe H, Kabius B, Urban K, Roas B, Klaumünzer S and Saemann-Ischenko G 1991 The influence of 173 MeV Xe-ion irradiation on the microstructure of $YBa_2Cu_3O_7$ thin films *Physica* C **179** 75–84

[17] Hua J, Welp U, Schlueter J, Kayani A, Xiao Z L, Crabtree G W and Kwok W K 2010 Vortex pinning by compound defects in $YBa_2Cu_3O_{7-\delta}$ *Phys. Rev.* B **82** 024505

[18] MacManus-Driscoll J L *et al* 2004 Strongly enhanced current densities in superconducting coated conductors of $YBa_2Cu_3O_{7-x} + BaZrO_3$ *Nat. Mater.* **3** 439–43

[19] Zhang Y, Rupich M W, Solovyov V, Li Q and Goyal A 2020 Dynamic behavior of reversible oxygen migration in irradiated-annealed high temperature superconducting wires *Sci. Rep.* **10** 14848

[20] Foreman A J E, Phythian W J and English C A 1992 The molecular dynamics simulation of irradiation damage cascades in copper using a many-body potential *Phil. Mag.* A **66** 671–95

[21] Phythian W, Stoller R, Foreman A, Calder A and Bacon D 1995 A comparison of displacement cascades in copper and iron by molecular dynamics and its application to microstructural evolution *J. Nucl. Mater.* **223** 245–61

[22] Van Brutzel L, Vincent-Aublant E and Delaye J-M 2009 Large molecular dynamics simulations of collision cascades in single-crystal, bi-crystal and poly-crystal UO_2 *Nucl. Instrum. Methods Phys. Res.* B **267** 3013–6

[23] Liu J, Vázquez Muíños H, Nordlund K and Djurabekova F 2020 Molecular dynamics simulation of the effects of swift heavy ion irradiation on multilayer graphene and diamond-like carbon *Appl. Surf. Sci.* **527** 146495

[24] Khara G S, Murphy S T, Daraszewicz S L and Duffy D M 2016 The influence of the electronic specific heat on swift heavy ion irradiation simulations of silicon *J. Phys.: Condens. Matter* **28** 395201

[25] Cui F, Xie J and Li H 1992 Preferential radiation damage of the oxygen sublattice in $YBa_2Cu_3O_{7-\delta}$: a molecular-dynamics simulation *Phys. Rev.* B **46** 11182

[26] Summers G, Burke E, Chrisey D, Nastasi M and Tesmer J 1989 Effect of particle-induced displacements on the critical temperature of $YBa_2Cu_3O_{7-\delta}$ *Appl. Phys. Lett.* **55** 1469–71

[27] Benzi P, Bottizzo E and Rizzi N 2004 Oxygen determination from cell dimensions in YBCO superconductors *J. Cryst. Growth* **269** 625–9

[28] Jorgensen J D, Veal B W, Paulikas A P, Nowicki L J, Crabtree G W, Claus H and Kwok W K 1990 Structural properties of oxygen-deficient $YBa_2Cu_3O_{7-\delta}$ *Phys. Rev.* B **41** 1863–77

[29] Jorgensen J D, Veal B W, Paulikas A P, Nowicki L J, Crabtree G W, Claus H and Kwok W K 1990 Erratum: structural properties of oxygen-deficient $YBa_2Cu_3O_{7-\delta}$ *Phys. Rev.* B **42** 995

[30] Kwok W K, Crabtree G W, Umezawa A, Veal B W, Jorgensen J D, Malik S K, Nowicki L J, Paulikas A P and Nunez L 1988 Electronic behavior of oxygen-deficient $YBa_2Cu_3O_{7-\delta}$ *Phys. Rev.* B **37** 106–10

[31] Rappe A K and Goddard W A III 1991 Charge equilibration for molecular dynamics simulations *J. Phys. Chem.* **95** 3358–63

[32] Van Duin A C, Dasgupta S, Lorant F and Goddard W A 2001 ReaxFF: a reactive force field for hydrocarbons *J. Phys. Chem.* A **105** 9396–409

[33] Chaplot S L 1990 Interatomic potential, phonon spectrum and molecular-dynamics simulation up to 1300 k in $YBa_2Cu_3O_{7-\delta}$ *Phys. Rev.* B **42** 2149–54

[34] Baetzold R C 1988 Atomistic simulation of ionic and electronic defects in $YBa_2Cu_3O_7$ *Phys. Rev.* B **38** 11304–12

[35] Sorbom B N 2017 The effect of irradiation temperature on REBCO J_c degradation and implications for fusion magnets *PhD Thesis* Massachusetts Institute of Technology

[36] Buckingham R A 1938 The classical equation of state of gaseous helium, neon and argon *Proc. R. Soc.* A **168** 264–83

[37] Born M and Mayer J E 1932 Zur gittertheorie der ionenkristalle *Z. Phys.* **75** 1–18

[38] Atkins P, De Paula J and Keeler J 2018 *Atkins' Physical Chemistry* (Oxford: Oxford University Press)

[39] Ewald P P 1921 Die berechnung optischer und elektrostatischer gitterpotentiale *Ann. Phys., Lpz.* **369** 253–87

[40] Ziegler J F and Biersack J P 1985 The stopping and range of ions in matter *Treatise on Heavy-Ion Science* (Berlin: Springer) pp 93–129

[41] Rushton M 2018 atsim.potentials—potential model tabulation for atomic scale simulation (available at: https://atsimpotentials.readthedocs.io/)

[42] Plimpton S 1995 Fast parallel algorithms for short-range molecular dynamics *J. Comput. Phys.* **117** 1–19

[43] Gale J D 1997 GULP: a computer program for the symmetry-adapted simulation of solids *J. Chem. Soc. Faraday Trans.* **93** 629–37

[44] Rushton M 2018 mjdrushton/potential-pro-fit (available at: https://github.com/mjdrushton/potential-pro-fit)

[45] Garrett A 2017 inspyred: bio-inspired algorithms in python (available at: http://aarongarrett.github.io/inspyred/)

[46] Clark S J, Segall M D, Pickard C J, Hasnip P J, Probert M I J, Refson K and Payne M C 2005 First principles methods using CASTEP *Z. Kristallogr.* **220** 567–70

[47] Payne M C, Teter M P, Allan D C, Arias T and Joannopoulos A J 1992 Iterative minimization techniques for *ab initio* total-energy calculations: molecular dynamics and conjugate gradients *Rev. Mod. Phys.* **64** 1045

[48] Perdew J P, Burke K and Ernzerhof M 1996 Generalized gradient approximation made simple *Phys. Rev. Lett.* **77** 3865

[49] Monkhorst H J and Pack J D 1976 Special points for Brillouin-zone integrations *Phys. Rev.* B **13** 5188

[50] Murphy S T 2020 A point defect model for $YBa_2Cu_3O_7$ from density functional theory *J. Phys. Commun.* **4** 115003

[51] Bjorkman T 2011 CIF2Cell: generating geometries for electronic structure programs *Comput. Phys. Commun.* **182** 1183–6
[52] Shinoda W, Shiga M and Mikami M 2004 Rapid estimation of elastic constants by molecular dynamics simulation under constant stress *Phys. Rev.* B **69** 134103
[53] Parrinello M and Rahman A 1980 Crystal structure and pair potentials: a molecular-dynamics study *Phys. Rev. Lett.* **45** 1196
[54] Parrinello M and Rahman A 1981 Polymorphic transitions in single crystals: a new molecular dynamics method *J. Appl. Phys.* **52** 7182–90
[55] Shanno D F 1970 Conditioning of quasi-newton methods for function minimization *Math. Comput.* **24** 647–56
[56] Fernandes A, Santamaria J, Bud'ko S, Nakamura O, Guimpel J and Schuller I K 1991 Effect of physical and chemical pressure on the superconductivity of high-temperature oxide superconductors *Phys. Rev.* B **44** 7601
[57] Lei M, Sarrao J, Visscher W M, Bell T, Thompson J, Migliori A, Welp U and Veal B 1993 Elastic constants of a monocrystal of superconducting $YBa_2Cu_3O_{7-\delta}$ *Phys. Rev.* B **47** 6154
[58] Lidiard A B 1989 The Mott–Littleton method: an introductory survey *J. Chem. Soc. Faraday Trans.* **85** 341–9
[59] Mehrer H 2007 *Diffusion in Solids: Fundamentals, Methods, Materials, Diffusion-Controlled Processes* (*Springer Series in Solid-State Sciences*) (Berlin: Springer)
[60] Jackson M L, Fossati P C M and Grimes R W 2016 Simulations of threshold displacement in beryllium *J. Appl. Phys.* **120** 045903
[61] Kinchin G H and Pease R S 1955 The displacement of atoms in solids by radiation *Rep. Prog. Phys.* **18** 1–51
[62] Norgett M, Robinson M and Torrens I 1975 A proposed method of calculating displacement dose rates *Nucl. Eng. Des.* **33** 50–54
[63] Sand A, Byggmästar J, Zitting A and Nordlund K 2018 Defect structures and statistics in overlapping cascade damage in fusion-relevant bcc metals *J. Nucl. Mater.* **511** 64–74
[64] Stukowski A 2009 Visualization and analysis of atomistic simulation data with OVITO–the open visualization tool *Modelling Simul. Mater. Sci. Eng.* **18** 015012
[65] Hartman S T, Mundet B, Idrobo J-C, Obradors X, Puig T, Gázquez J and Mishra R 2019 Direct observation of apical oxygen vacancies in the high-temperature superconductor $YBa_2Cu_3o_{7-x}$ *Phys. Rev. Mater.* **3** 114806
[66] Horide T and Matsumoto K 2014 Anisotropic strain dependence of oxygen vacancy formation in $YBa_2Cu_3O_{7-\delta}$: first principle study *Supercond. Sci. Technol.* **27** 115013
[67] Stoneham A and Smith L 1991 Defect phenomena in superconducting oxides and analogous ceramic oxides *J. Phys.: Condens. Matter.* **3** 225
[68] Vázquez-Navarro M D 1998 A thermogravimetric study of oxygen diffusion in $YBa_2Cu_3O_{7-\delta}$ *PhD Thesis* University of Cambridge
[69] Yamaji A, Maeno S, Tomizawa M, Arai M and Adachi T 2000 Oxygen-ion diffusion in $YBa_2Cu_3O_{7-x}$ ceramics *Physica* C **335** 264–7
[70] Tolpygo S K, Lin J-Y, Gurvitch M, Hou S Y and Phillips J M 1996 Effect of oxygen defects on transport properties and T_c of $YBa_2Cu_3O_{6+\delta}$: displacement energy for plane and chain oxygen and implications for irradiation-induced resistivity and T_c suppression *Phys. Rev.* B **53** 12462–74
[71] Piñera I, Cruz C M, Abreu Y and Leyva A 2007 Determination of atom displacement distribution in YBCO superconductors induced by gamma radiation *Phys. Status Solidi* a **204** 2279–86
[72] Frischherz M, Kirk M, Farmer J, Greenwood L and Weber H 1994 Defect cascades produced by neutron irradiation in $YBa_2Cu_3O_{7-\delta}$ *Physica* C **232** 309–27
[73] Martin G, Garcia P, Van Brutzel L, Dorado B and Maillard S 2011 Effect of the cascade energy on defect production in uranium dioxide *Nucl. Instrum. Methods Phys. Res.* B **269** 1727–30
[74] Sahi Q and Kim Y-S 2018 Primary radiation damage characterization of α-iron under irradiation temperature for various PKA energies *Mater. Res. Express* **5** 046518
[75] Nordlund K *et al* 2018 Primary radiation damage: a review of current understanding and models *J. Nucl. Mater.* **512** 450–79